Copyright Notice

Bayesian Cooperative Relative Vehicle Positioning using Pseudorange Differences

Fabian de Ponte Müller, Estefania Munoz Diaz, Bernhard Kloiber and Thomas Strang
German Aerospace Center - DLR
Institute of Communications and Navigation
Wessling, Germany
Email: fabian.pontemueller@dlr.de

***Abstract*—Forward collision warning systems, lane change assistants or cooperative adaptive cruise control are examples of safety relevant applications that rely on accurate relative positioning between vehicles. Current solutions estimate the position of surrounding vehicles by measuring the distance with a RADAR sensor or a camera system. The perception range of these sensors can be extended by the exchange of GNSS information between the vehicles using an inter-vehicle communication link. In this paper we analyze two competing strategies against each other: the subtraction of the absolute positions estimated in each vehicle and the differentiation of GNSS pseudoranges. The aim of the later approach is to cancel out correlated errors in both receivers and, thus, achieve a better relative position estimate. The theoretical analysis is backed with Monte-Carlo simulations and empirical measurements in real world scenarios. Further on, two Bayesian approaches that make use of pseudorange differences are proposed. In a Kalman Filter pseudorange and Doppler measurements are used to estimate the baseline between two vehicles. This is extended in a second filter using on-board inertial and speed sensors following a multisensor fusion approach. The performance is evaluated in both, a highway and an urban scenario. The multisensor fusion approach proves to be able to stabilize the baseline estimate in GNSS challenging environments, like urban canyons and tunnels.**

Keywords*—*Vehicle Relative Positioning, Pseudorange, Doppler, Inertial Measurement Unit, Kalman filter

I. Introduction

Advanced Driver Assistance Systems play an important role in increasing the safety on today's roads while the knowledge about other vehicle's position is a fundamental prerequisite for numerous safety critical applications in the intelligent transportation system domain. Forward collision warning systems, lane change assistants or adaptive cruise control are examples of safety relevant applications that rely on accurate relative localization of surrounding vehicles.

Current solutions estimate the position of surrounding vehicles by measuring the distance with a radar, laser scanner or a camera system. However, all three solutions have a limited perception range, only detecting objects in their line-of-sight (see Fig. 1). The limited perception range of these sensors can be extended and enhanced by the use of cooperative approaches. In recent years big steps in the standardization of inter-vehicle communication have been achieved in Europe, North America and Japan. The standards IEEE802.11p or ITS-G5 allow exchanging information directly between vehicles up to a range of several hundreds of meters.

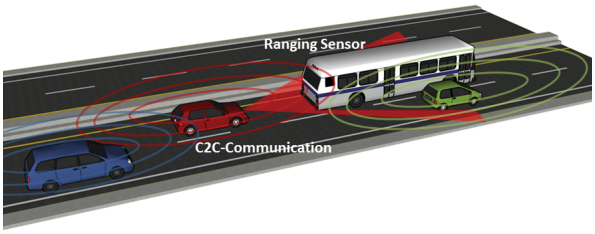

Fig. 1. Cooperative approaches based on direct communication between vehicles are able to extend the perception range of the ego-vehicle beyond the line-of-sight of current ranging sensors.

The European Telecommunications Standards Institute (ETSI) is currently working on the definition of different safety critical messages for the European Car-to-Car technology. Each vehicle will transmit periodically Cooperative Awareness Messages (CAM) [1] containing basic information such as position, speed and heading. The position in global coordinates can be used by a vehicle to estimate its neighbors' positions. The own coordinates might be estimated using a Global Navigation Satellite System (GNSS), like the American GPS System or the European Galileo system. This estimate can be additionally enhanced by supporting it with on-board inertial sensors or odometers.

A further possibility, though not standardized, is to exchange GNSS raw measurements among the vehicles and estimate the baseline vector between the receiver antennas by differentiation. This approach is analogous to Differential GPS (DGPS), where a static base station transmits correction data to nearby located rover stations. However, in the raw GNSS differential approach for vehicles, none of the nodes has the predominant role of the base station. The advantage of a raw GNSS differential approach is that correlated errors in both receivers are expected to cancel out.

Several research groups have extended the concept of pseudorange differentiation to vehicles by moving from the classic base station/rover setup for absolute position towards a two-rover setup for relative position estimation. Richter et al. introduce a relative localization approach on the basis of the exchange of GNSS pseudorange data in [2]. They formulate the mathematical problem but their work is not backed by real-world measurements. Yang et al. [3] propose an epoch-by-epoch weighted least squares method with pseudorange double differences to estimate a baseline between two antennas. Experimental results with static 3 meters and 8 meters baseline on

a rooftop yield mean baseline length errors of around 3 meters and maximum baseline length errors up to 40 meters. In [4], Alam et al. also present a cooperative positioning approach based on pseudorange double differences. Their simulations compare the distance estimated using this approach to stand-alone GPS. They also show real-world measurements with a static baseline and compare the results to the absolute position estimate. Later, in [5], the same group integrate pseudorange double differences from two vehicles into a Kalman filter and perform real-world tests in a sub-urban environment, yielding a baseline standard deviation error of 3.4 meters for a 12 minutes run. In [6], Obst et al. present a relative position estimator with an Unscented Kalman Filter (UKF) based on a constant turn rate model for the vehicle movement and pseudorange single differencing. Unfortunately, their analysis is not backed with measurements in dynamic scenarios. In [7] the authors present a sound analysis of a zero-baseline experiment in a controlled environment. Two ublox receivers were connected to a Spirent GNSS simulator in a zero-baseline configuration. The main goal was to validate the pseudorange double difference approach in a controlled environment by activating different types of error sources, such as noise, atmospheric delays and multipath. The problem of receiver synchronization was solved by extrapolating the pseudorange measurements from both receivers to a common point in time.

A number of research groups have addressed the relative positioning problem of vehicles by solving differenced carrier phase ambiguities rather than using differenced pseudorange techniques [8], [9], [10]. In order to obtain a highly precise relative position estimate with this technique the differenced integer number of cycles has to be resolved. This task, however, is time consuming, computationally heavy and specially difficult in vehicular environments due to signal disturbances, satellite blockage and multipath, which lead to cycle slips that will reset the resolution algorithm.

This paper aims at analyzing a raw GNSS differential approach based on code pseudorange double differences. By means of a theoretical-simulative analysis, we compare this pseudorange differencing (PRD) technique to the absolute position differencing (APD) approach to understand under which circumstances PRD outperforms APD. Unlike in [4], we will analyze the three dimensional position error in dependance of the number of satellites, the satellite geometry and the magnitude of common errors. For the real- world tests we present two Bayesian approaches. The first one is a GNSS-only approach, where the relative position to a foregoing vehicle is estimated from differenced pseudoranges using a Kalman filter (PRD-KF). In addition to [5], we add Doppler measurements to improve the dynamics of the filter. The second is a sensor fusion (MSF) design, where the former GNSS-only solution is supported by on-board sensors. The results with two moving vehicles in two different scenarios are presented.

This paper is structured as follows: in the following section the estimation of the baseline through the differentiation of absolute positions and through pseudorange double differences is presented. The performance of both estimators is compared theoretically and by simulations in Section III. Section IV describes two implementations to estimate the relative position of a foregoing vehicle using a Kalman filter and additional sensors. Section V presents the measurements performed with two test vehicles in different environments. Finally, Section VI presents the conclusions of this work.

II. Vehicle Baseline Estimation

The relative position of a target vehicle towards the ego or own vehicle is given by its baseline vector $\vec{b}$. In this paper, and for simplicity reasons, we will define the baseline as the space vector pointing from the GNSS antenna of the ego vehicle to the GNSS antenna of the target vehicle. It is possible to define this baseline vector in a global coordinate frame, as for instance an Earth-centered Earth-fixed (ECEF) frame, a local coordinate frame, as for instance an East-North-Up (ENU) frame, or a coordinate frame attached at the ego vehicle. In this work we assume that the coordinates of the baseline vector are given in an ENU frame.

The aim is to estimate this baseline vector between both GNSS antennas as accurately as possible. A GNSS receiver in each vehicle is able to measure the distance between its antenna and each of the tracked satellites. A pseudorange is an estimation of the range between the antennas of the satellite orbiting the Earth and the receiver on the ground. The range is attained by measuring the propagation time through the atmosphere of a signal transmitted by the satellite. Since a receiver is usually equipped with an inexpensive, inaccurate and unsynchronized oscillator, the measured distance is offset by an unknown amount. Additionally, the pseudorange is also corrupted by a series of errors produced at the satellite, the atmosphere or the receiver. The measured pseudorange ρ_i^k of a receiver i towards a satellite k can be modeled as follows:

$$\rho_i^k = R_i^k + \epsilon_\rho \tag{1}$$

where R_i^k is the true receiver-to-satellite geometric range and ϵ_ρ is the pseudorange error, both in meters. The pseudorange errors are divided in different terms corresponding to the different error sources:

$$\epsilon_\rho = \epsilon_{sat} + \epsilon_{user} + \epsilon_{ephem} + \epsilon_{ion} + \epsilon_{trop} + \epsilon_{mp} + \epsilon_{nm}, \tag{2}$$

where:

- **Satellite Clock Error** (ϵ_{sat}): this term represents the error in the signal transmission time due to the satellite on-board clock. Each satellite is equipped with an atomic clock. Although atomic clocks are highly accurate, their errors are large enough to require correction and must be taken into account. The satellite clock error is typically less than 1ms and varies slowly.
- **Receiver Clock Error** (ϵ_{user}): likewise, the receiver clock error must be included in the pseudorange error model. Receivers incorporate a quartz crystal oscillator that is far less accurate than the atomic clocks on board of the satellites. This error also includes the instrumental delay caused by the antenna, cables and filters.
- **Ephemeris Error** (ϵ_{ephem}): to calculate the receiver position the position of each satellite needs to be known. The calculation of satellite position is made by using orbital parameters broadcasted in the ephemeris data. Errors in satellite position when calculated from

the ephemeris data are represented as an additional delay error term in the measured pseudorange.

- **Tropospheric Error** (ϵ_{trop}): the lower part of the Earth's atmosphere is composed of dry gases and water vapor which produce a delay error in the GNSS signal's propagation time in comparison to a vacuum environment. Thus, the measured pseudorange is larger than the correct value. This error depends on the path the signal has to travel through the atmosphere and therefore depends on the satellite elevation angle.
- **Ionospheric Error** (ϵ_{ion}): the ionosphere consists of gases that are ionized by solar radiation. The ionization produces clouds of free electrons that act as a dispersive medium for GNSS signals in which propagation velocity is a function of frequency. Ionospheric delay error varies over time in a daily cycle and, just as well as the tropospheric error, are highly dependent of the satellite elevation angle.
- **Multipath Error** (ϵ_{mp}): objects in the vicinity of a receiver antenna may cause reflections of GNSS signals resulting in one or more secondary propagation paths. These secondary-path signals always have a longer propagation time and can significantly distort the amplitude and phase of the direct-path signal. In case the LOS component is blocked by the environment the correlators might track a secondary path causing a large error in the estimation.
- **Non-modeled Error** (ϵ_{nm}): this term collects all the non-modeled remaining errors and noise.

A. Absolute Position Differencing - APD

In this work we will call the state of the art approach Absolute Position Differencing (APD). After acquiring and tracking the GNSS signal of at least four satellites, a GNSS receiver i is able to compute an estimate of its three dimensional absolute position vector $p_i = [x_i \quad y_i \quad z_i]^T$. The straight forward approach in this case consists in solving the position and the receiver clock error ϵ_{user} in a non-linear system of equations that takes all available pseudorange measurements into account. The equation resulting from the pseudorange measurement from receiver i to satellite k is:

$$\rho_i^k = \sqrt{(x^k - x_i)^2 + (y^k - y_i)^2 + (z^k - z_i)^2} + \epsilon_{user},$$

where $\begin{bmatrix} x^k & y^k & z^k \end{bmatrix}^T$ are the satellite coordinates. The resulting system of non-linear equations can be solved by applying the Newton-Raphson method iteratively on

$$\delta\rho = G_u \cdot \delta x, \tag{3}$$

starting with an approximate initial user position and clock bias x_0, calculating the offset δx and repeating until the algorithm converges [11]. The geometry matrix G_u contains the unitary vectors to the satellites in view as row vectors and a last column filled with ones. This iterative least squares method will reach the solution $\hat{p}_i$ and $\hat{\epsilon}_{user}$ that minimizes the root mean squared error to all pseudoranges. For our following performance analysis, we define the geometry matrix for APD as:

$$G_{APD} = (G_u \cdot G_u^T)^{-1} \cdot G_u^T. \tag{4}$$

Several approaches exist to improve the absolute position estimated in this way. A weighted least squares (WLS) approach can be used to give different weights to the measurements according to some parameter, as for instance, the elevation of the satellite or the carrier-to-noise ratio of the received signal. Some of the mentioned error sources can be modeled and be partially subtracted to the pseudorange measurements in order to decrease their impact on the final position estimate. Satellite based augmentation systems (SBAS), like the European EGNOS or the American WAAS, broadcast correction data for the pseudorange measurements that have been previously computed by a network of base stations. In a similar way, DGPS is able to better estimate the pseudorange correction using a nearby located base station. Kalman filters or similar Bayesian approaches make use of the temporal relationship of the unknowns and the biases and use these to increase the accuracy of the position estimate.

In APD the estimate $\hat{b}_{APD}$ of the baseline $\vec{b}_{ij}$ between two receivers i and j is calculated in the following way:

$$\hat{b}_{APD} = \hat{p}_j - \hat{p}_i.$$

In the following section we will analyze how, and under which circumstances, this estimate of the baseline is influenced by the above mentioned ranging errors.

B. Pseudorange Differencing - PRD

The Pseudorange Differencing (PRD) approach for relative positioning of vehicles relies on the double differentiation of pseudorange measurements. In a first step, a single difference measurement $\Delta\rho_{ij}^k$ is obtained by subtracting the pseudorange measurements from two different receivers referred to the same satellite k. Under a close proximity assumption, the single difference operation nearly cancels out the terms ϵ_{ion}, ϵ_{trop} and ϵ_{ephem}, as well as the satellite clock error ϵ_{sat}, that is canceled out completely. By subtracting two single differences towards two different satellites k and l, a double difference measurement $\nabla\Delta\rho_{ij}^{kl}$ is computed. With this procedure, the common errors to both satellites, ϵ_{user}, are canceled out. A double difference pseudorange measurement is expressed in the following way:

$$\nabla\Delta\rho_{ij}^{kl} = \nabla\Delta R_{ij}^{kl} + \nabla\Delta\epsilon_\rho, \tag{5}$$

where the symbol $\nabla\Delta$ denotes the difference between the corresponding terms in the two single differences. $\nabla\Delta R_{ij}^{kl}$ is the projection of the baseline in the differenced direction to satellites k and l. The error term $\nabla\Delta\epsilon_\rho$ represents the remaining differential error term between two receivers and two satellites:

$$\nabla\Delta\epsilon_\rho \approx \nabla\Delta\epsilon_{mp} + \nabla\Delta\epsilon_{nm}.$$

As reported in [7], the remaining errors are mainly multipath and non-modeled errors like thermal noise and interference. It should be noticed that, while common errors terms are

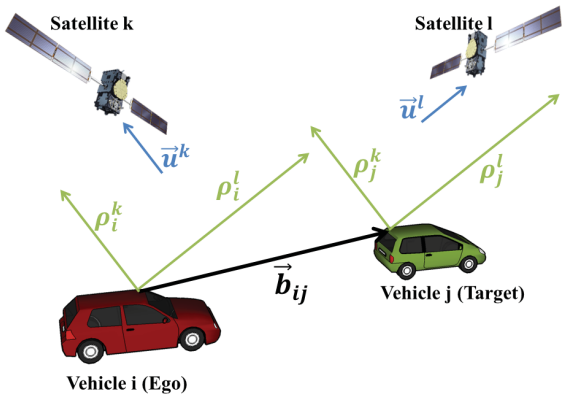

Fig. 2. Relationship between the baseline between two vehicles and the pseudorange double difference measurements.

nearly canceled out by differencing, uncorrelated error terms are increased with this operation likewise.

Fig. 2 shows the geometric relationship between the vehicles and the satellites. The baseline $\vec{b}_{ij}$ between two vehicles, ego and target, is a vector in space expressed in a certain coordinate frame. Each double difference measurement $\nabla\Delta\rho_{ij}^{kl}$ is the projection of the baseline vector $\vec{b}_{ij}$ in the direction of the differenced satellite unitary vector $\vec{u}^{kl} = \vec{u}^k - \vec{u}^l$. By taking three or more double difference measurements the baseline coordinates can be computed by resolving the following system of linear equations:

$$\begin{bmatrix} \nabla\Delta\rho_{ij}^{kl} \\ \nabla\Delta\rho_{ij}^{km} \\ \nabla\Delta\rho_{ij}^{kn} \end{bmatrix} = \begin{bmatrix} u_x^{kl} & u_y^{kl} & u_z^{kl} \\ u_x^{km} & u_y^{km} & u_z^{km} \\ u_x^{kn} & u_y^{kn} & u_z^{kn} \end{bmatrix} \begin{bmatrix} b_x \\ b_y \\ b_z \end{bmatrix}.$$

The compact representation for this linear system of equations is given by:

$$\nabla\Delta\rho_{ij} = G_{uu} \cdot \vec{b}_{ij}, \tag{6}$$

where G_{uu} is the geometry matrix containing differenced unitary vectors to the satellites in view. For future analysis we define the geometry matrix for PRD as:

$$G_{PRD} = (G_{uu} \cdot G_{uu}^T)^{-1} \cdot G_{uu}^T. \tag{7}$$

Usually, the system of linear equations in Eq. 6 is overdetermined. The solution $\hat{b}_{PRD}$ that minimizes the squared error to this system of equations is given by [12]:

$$\hat{b}_{PRD} = (G_{uu} \cdot G_{uu}^T)^{-1} \cdot G_{uu}^T \cdot \nabla\Delta\rho_{ij}.$$

Each double difference noise component $\nabla\Delta\epsilon_\rho$ in Eq. 6 includes the noise contributions from four pseudorange measurements, ρ_i^k, ρ_j^k, ρ_i^l and ρ_j^l. Under the assumption of mutually independent and equally distributed noise with standard deviation σ_ρ on each pseudorange, we can write the noise variance-covariance matrix of the pseudorange double differences as follows:

$$R_{\nabla\Delta\rho} = 2\sigma_\rho^2 \begin{bmatrix} 2 & 1 & \dots & 1 \\ 1 & 2 & \dots & 1 \\ \vdots & & \ddots & \vdots \\ 1 & 1 & \dots & 2 \end{bmatrix}. \tag{8}$$

From Eq. 8 we learn that the noise variance for a double difference measurement is four times the noise variance of each pseudorange measurement (assuming equal variance on all pseudorange measurements). Further on, it should be noticed that the resulting double differenced observations involving a common satellite are statistically dependent. Therefore, the calculated remaining noise variance-covariance matrix $R_{\nabla\Delta\rho}$ is not diagonal, but has off-diagonal components of twice the noise variance of the pseudorange measurement.

The additional data that needs to be transmitted in PRD is in the order of the current CAM message length on data link layer. Disregarding any special type of coding and using four Bytes to encode each pseudorange measurement, less than 100 Byte need to be transmitted in order to exchange timestamped pseudoranges, carrier-to-noise ratio and satellite number between the vehicles. The usual CAM message size assumed in the literature ranges from 200 Byte to 500 Byte [13], [14].

In the following section we show how the ranging errors on the pseudorange measurements in both receivers propagate to the baseline estimate in both, APD and PRD.

III. Performance Analysis

The previous section has introduced two different techniques to estimate the baseline vector between two vehicles, namely, the subtraction of absolute positions (APD) and the differentiation of GNSS pseudoranges (PRD). In this section we perform a systematic analysis of both approaches. To simplify this analysis we assume a single epoch view, where a temporal relationship of the errors is neglected. The metric used in this work is the mean squared error, which includes both, the variance and the bias of the estimator. The mean squared error (MSE) for our problem is defined as $MSE = E[\left\|\hat{b} - \vec{b}\right\|^2]$. The input to our estimators are the pseudoranges ρ_i^k. The error model considered for the pseudoranges is the following:

$$\epsilon_{\rho_i^k} = C^k + n_i^k, \tag{9}$$

where C^k is the common error to the pseudoranges of both receivers i and j to the same satellite k. For simplicity, we assume the common error to be uniformly distributed in the interval $[0, c]$, where c is the common error limit. A uniformly distribution was chosen since the atmospheric errors are always positive and represent the largest contribution to the error budget, while satellite clock and satellite position errors are of changing sign and centered around zero. The concrete distribution of the error is however not important for the following analysis. The statistical properties of C^k are

summarized next:

$$C_i^k = C_j^k$$
$$E[C^k] = \frac{c}{2}$$
$$E[(C^k)^2] = \frac{c^2}{3}$$
$$E[C^k \cdot C^l] = E[C^k] \cdot E[C^l] = \frac{c^2}{4}$$

n_i^k in Eq. 9 is a noise component following a Gaussian distribution with zero mean, equal variance on all satellites and mutually independent between satellites and between receivers. Its properties are summarized next:

$$E[n_i^k] = 0$$
$$E[(n_i^k)^2] = \sigma_\rho^2$$
$$E[n_i^k \cdot n_j^k] = 0$$
$$E[n_i^k \cdot n_i^l] = 0$$

It should be noticed that we do not make any assumptions on the time correlation of the errors since we are doing a snapshot analysis. Only to mention that both, the common error and the noise, are in general not white but have a certain time correlation. The common error is, to a certain extend, static due to the limited dynamic of the satellite position, the dynamic of the atmosphere or the behavior of the atomic clocks on the satellite. The noise component on the pseudoranges is colored by the tracking loops in the receivers. Now, we will see how these errors propagate from the pseudoranges to both baseline estimators, APD and PRD. On the one hand, we have the baseline estimate $\hat{b}_{APD}$ with a mean squared error MSE_{APD}. It can be mathematically derived that the MSE for APD is given by:

$$\begin{aligned} MSE_{APD} =& E[\left\|\hat{b}_{APD} - \vec{b}\right\|^2] = \\ &= G^e_{APD} \cdot R_\rho \cdot G^{eT}_{APD} + G^t_{APD} \cdot R_\rho \cdot G^{tT}_{APD} \\ &- 2 \cdot G^e_{APD} \cdot R_C \cdot G^{tT}_{APD} \end{aligned} \quad (10)$$

The geometry matrices from Eq. 4 at the ego receiver, G^e_{APD} , and at the target receiver,G^t_{APD}, transform the pseudorange errors given by the covariance matrices R_ρ and R_C into an error in the baseline. Considering the error distributions and statistical properties, the covariance matrices are defined as:

$$R_\rho = \begin{bmatrix} \sigma^2 + \frac{c^2}{3} & \frac{c^2}{4} & \cdots & \frac{c^2}{4} \\ \frac{c^2}{4} & \sigma^2 + \frac{c^2}{3} & \cdots & \frac{c^2}{4} \\ \vdots & & \ddots & \vdots \\ & \cdots & & \end{bmatrix},$$

$$R_C = \begin{bmatrix} \frac{c^2}{3} & \frac{c^2}{4} & \cdots & \frac{c^2}{4} \\ \frac{c^2}{4} & \frac{c^2}{3} & \cdots & \frac{c^2}{4} \\ \vdots & & \ddots & \vdots \\ & \cdots & & \end{bmatrix}.$$

On the other hand, we have the baseline estimate $\hat{b}_{PRD}$, whose mean squared error is MSE_{PRD}.

$$MSE_{PRD} = E[\left\|\hat{b}_{PRD} - \vec{b}\right\|^2] = G_{PRD} \cdot R_{\nabla\Delta\rho} \cdot G^T_{PRD} \quad (11)$$

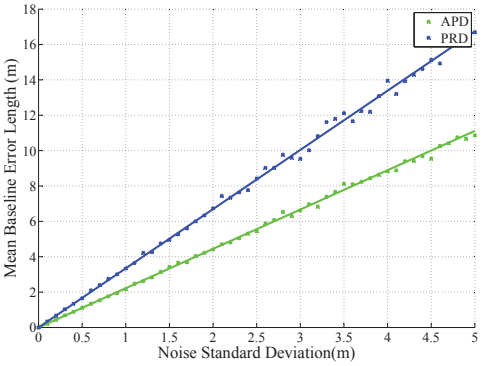

Fig. 3. Baseline error of APD and PRD with pseudoranges corrupted by noise. In PRD the noise contribution is multiplied by four yielding in general a higher baseline error. The mean baseline error contains also the impact of the geometric properties of the problem.

G_{PRD} is the transformed geometry matrix from Eq. 7 and $R_{\nabla\Delta\rho}$ is the error covariance matrix for the double differences from Eq. 8. The later contains only the contribution from the noise term n_i^k, as the common error C_i^k cancels out.

Finally, with Eq. 10 and Eq. 11 we have found the mean squared error for both estimators in dependence of the geometry of the constellations used in each receiver and the common error limit c and the noise standard deviation σ_ρ.

In the following, we will make use of these equations to test under which assumptions which estimator outperforms the other. Given a fixed arbitrary constellation of 12 GNSS satellites and two antenna positions separated 100 meters from each other, a series of Monte-Carlo simulations have been performed using MATLAB in order to determine the performance of each of the methods. For this purpose, multiple runs with varying random errors on the pseudoranges have been simulated. The pseudorange of each receiver to each satellite is the true range, plus a bias term due to the user clock and an error term. The simulations are performed in a local coordinate frame centered at the ego receiver. In APD, each receiver estimates its position and user clock bias by solving iteratively the non-linear least squares problem. In a second step the positions in the local frame are subtracted from each other to retrieve the baseline. In PRD, first the common set of pseudoranges are subtracted twice to calculate the pseudorange double differences. The baseline using all double differences is estimated, using MATLAB's least squares function. The mean squared error vector over all simulations is computed in order to compare both methods against each other.

First, a simulation adding a random Gaussian error n_i^k with a certain standard deviation σ_ρ on each of the pseudoranges has been performed. The resulting baseline's mean squared error is shown in Fig. 3. The doted or ragged curves in the subsequent figures are the results from the Monte-Carlo simulation, whereas the solid lines and planes correspond to the theoretical results from Eq. 10 and Eq. 11. This proves that our theoretical derived equations correctly describe the errors in the scenario. It can be seen that APD always yields a better solution than PRD. This is due to the fact that PRD's estimate is subjected to four times the pseudorange noise on the code

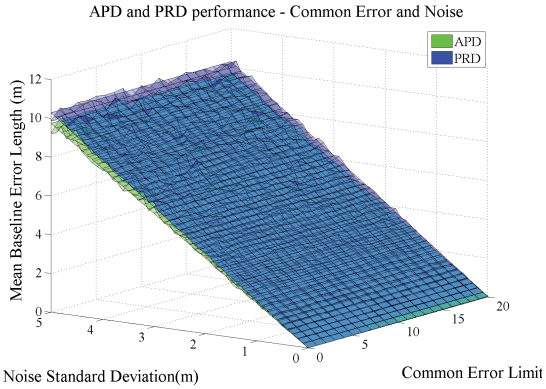

Fig. 4. Baseline error of APD and PRD with pseudoranges corrupted by common errors uniformly distributed between zero and the common error limit. In APD both receivers use the same set of satellites. In this case both, PRD and APD, cancel out correctly the common errors.

double differences. If the number of satellites is decreased the solutions of APD and PRD tend to be similar and are exactly the same when using the same four satellites.

Next, common errors are added on the pseudoranges of ego and target receiver. The 3-D plot in Fig. 4 displays the baseline mean squared error in dependance of both, the noise standard deviation σ_ρ and the common error limit c. It can be seen how, independently on the magnitude of the common error, APD performs better than PRD. When the same satellites are used at both receivers, the bias in $\hat{p}_i$ and $\hat{p}_j$ is equal and cancels out. In this case, both estimators, APD and PRD, are able to cancel out common errors, but APD achieves a lower variance. This is however not the case when a different subset of satellites is used in each receiver. Fig. 5 shows the baseline error when using ten common and one different satellite in each receiver. The result is a baseline error of several meters in APD. This leads to the conclusion that, depending on the magnitude of the noise and the magnitude of the common errors on the pseudoranges, APD or PRD will give a better result for the estimation of the baseline. The red line on the error plane is the APD-PRD performance threshold that shows the limit at which noise and common errors compensate and the APD and the PRD planes intersect.

The presented results were simulated taking a fixed constellation of satellites in the sky. Since the GPS satellite constellation repeats approximately every day, we have extended the simulation to 24 hours in order to attain for all possible positions of the satellites. In the same way, we tested the performance of both approaches using different number of satellites in every receiver. The resulting displacement of the APD-PRD performance threshold is shown in Fig. 6. The figure reveals that indeed the performance of both approaches depends on the constellation geometry and on the number of used satellites. We see that there areas of the error plane where PRD outperforms APD and vice versa. For example, when the noise standard deviation is below 0.5 m and the common errors are distributed between 0 m and 10 m PRD yields a better baseline estimate than APD when using more than 6 satellites.

This performance analysis yields that in the case of noise errors APD approach yields smaller baseline estimate errors

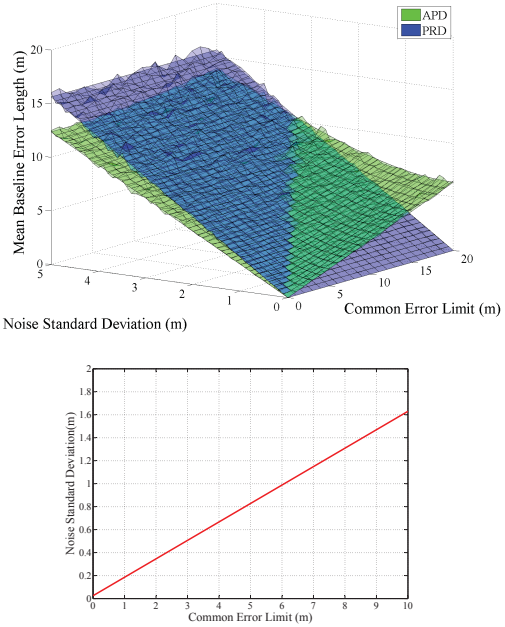

Fig. 5. The upper figure shows the baseline error of APD and PRD with pseudoranges corrupted by noise and common errors. For APD the receivers use each 11 satellites where ten are common. PRD uses ten common satellites. It can be noticed how the common errors degrade APD's baseline estimate. The lower figure shows the APD-PRD performance threshold. It is the projection of the intersection between both planes onto the error plane.

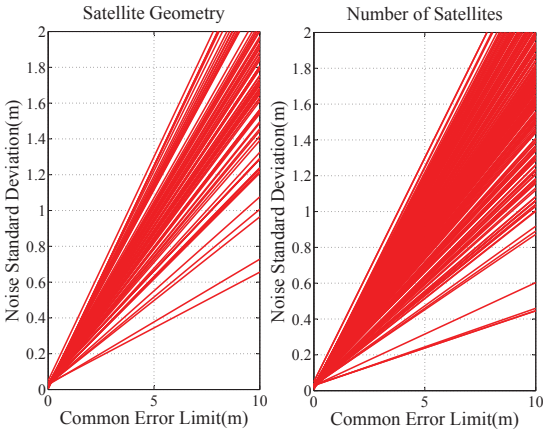

Fig. 6. The performance threshold in dependence of the pseudorange noise standard deviation and the common error limit is shown. The left figure shows the results for 10 common satellites during one whole day. The right figure are the results for combinations of 6 to 11 out of 12 satellites in each receiver.

than PRD. This comes from the fact that the subtraction of pseudoranges in the PRD approach doubles the variance of the errors in the measurements that are used in the baseline least square problem. When looking at the common errors, it can be observed that, when using the same set of satellites at both receivers, the APD solution also cancels out common errors at both receivers. When using different satellites at each receiver, APD's performance decreases with increasing common errors. The performance of each of the estimators will ultimately depend on the working point of the receiver in the scenario. In an open sky environment with good GNSS signal coverage the errors due to noise will be small. Signal blockage, however, might cause a drop in the received signal strength and, therefore, a sudden increase in the noise variance. Measurements performed by the authors in a controlled environment with a Spirent GNSS Simulator and with the same ublox receivers used in this work revealed that the noise on the pseudoranges above a carrier-to-noise ratio of 30 dBHz was below 25 cm [7]. On the other hand, the magnitude of common errors existing on the pseudoranges depends on the approach used to combat them. A first approach is to use the broadcasted parameters in the navigation message to compute the satellite clock and satellite position. The atmospheric delay caused by the ionosphere and the troposphere can be partly canceled using models with static (troposphere) and broadcasted (ionosphere) parameters. SBAS and DGPS, as already mentioned, could further reduce the impact of common errors.

IV. Multisensor Fusion for Relative Positioning

In this section we present a novel approach for the estimation of the relative position of two vehicles on the basis of GNSS pseudorange and Doppler double differences. In a second step, and, in order to stabilize this estimation in GNSS degraded scenarios, the measurements from on-board sensors are incorporated into the estimate.

To track the relative position of two vehicles we choose a probabilistic filtering technique based on Bayesian filters. The Kalman filter (KF) is one possible technique to implement a dynamic Bayesian filter. Here, the posterior probability of the state of the system at time step k is described by its mean x^k and its covariance matrix P^k. In the prediction step a prior distribution for the state is predicted according to the following equation

$$x^k = f(x^{k-1}) + \nu^k$$

where $f(\cdot)$ is the prediction function that transforms the mean of the estimate. The system noise ν^k, which represents the uncertainty in the prediction, is modeled as zero-mean Gaussian noise with covariance Q. The prior distribution of the state is updated with new measurements z^k in the update step to find its posterior distribution according to the following equation.

$$z^k = h(x^k) + \eta^k$$

The transformation from the estimation space to the measurement space is done through function $h(\cdot)$. The observation noise η^k is modeled as a zero-mean Gaussian with covariance matrix R. Under the assumptions that the functions $f(\cdot)$ and $h(\cdot)$ are linear and that the noises ν and η are Gaussian, it can be ensured that the posterior probability function of the state is always Gaussian and that the Kalman filter is the optimal solution to the estimation problem. In the case that the functions $f(\cdot)$ and $h(\cdot)$ are not linear or the noise probability distributions are not Gaussian, approximations to the optimal solution exist, such as the Extended Kalman filter (EKF) or the Unscented Kalman filter (UKF).

A. PRD Kalman Filter

For relative positioning we are interested in estimating the baseline vector between two vehicles. The three-dimensional baseline vector points from the ego to the target vehicle and can be written in ENU-coordinates as $\vec{b} = \begin{bmatrix} b_E & b_N & b_U \end{bmatrix}^T$. For the purpose of our work we are only interested in estimating the east and the north components. Along with the two-dimensional baseline vector we will also estimate the change in the baseline vector, i.e. the relative speed of the vehicles. Our state vector is:

$$x^k = \begin{bmatrix} b_E & b_N & \dot{b}_E & \dot{b}_N \end{bmatrix}^T.$$

A first order constant velocity model is used to predict the baseline from time step k to time step $k+1$:

$$x^{k+1} = \begin{bmatrix} 1 & 0 & \Delta T & 0 \\ 0 & 1 & 0 & \Delta T \\ 0 & 0 & 1 & 0 \\ 0 & 0 & 0 & 1 \end{bmatrix} x^k + \nu, \tag{12}$$

where ΔT is the time between the time steps. In the update step the predicted state is updated with the measurements from the GNSS receiver. The pseudorange and Doppler measurements from the ego and target receiver taken at approximately the same time are synchronized [7] and double differences are formed. These measurements update the state through the geometry matrix G_{uu} from Section II.

$$\nabla\Delta\rho = G_{uu} \cdot \begin{bmatrix} b_E & b_N \end{bmatrix}^T + \eta_\rho \tag{13}$$

$$\nabla\Delta\dot{\Phi} = G_{uu} \cdot \begin{bmatrix} \dot{b}_E & \dot{b}_N \end{bmatrix}^T + \eta_{\dot{\Phi}} \tag{14}$$

The observation noise η_ρ and $\eta_{\dot{\Phi}}$ of the pseudorange and Doppler measurements is modeled as zero-mean Gaussian noise with covariance matrices R_ρ and $R_{\dot{\Phi}}$, correspondingly. The covariance matrices are calculated from the carrier-to-noise ratios estimated in the receiver. Since the equations for prediction and update are linear in the state variables we will implement this estimation problem as a KF. By tuning the prediction noise covariance matrix Q in relationship to R_ρ and $R_{\dot{\Phi}}$ the smoothing capability of the filter can be controlled. In Section V we will see how this filter performs in real-world dynamic scenarios. It will be compared to the epoch-by-epoch estimation of the baseline with PRD.

B. Multisensor Fusion

A second filter is proposed to stabilize the first one in degraded GNSS environments, such as tree covered roads or urban canyons. The approach is also suited for GNSS denied environments like tunnels. The main idea is to take the advantage of the long term stability in relative positioning offered by GNSS pseudorange and Doppler double differences and add the short term stability of on-board sensors. While the GNSS measurements might be temporary impaired by multipath errors, speedometers and turn rate sensors inside the

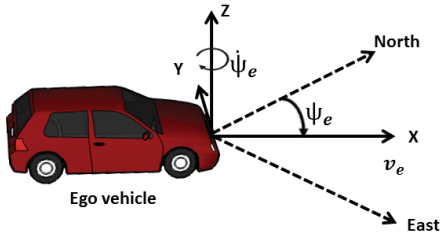

Fig. 7. This figure shows the vehicle coordinate system X,Y,Z in the local coordinate system ENU. v_e is the speed of the vehicle, ψ_e is its heading vector and $\dot{\psi}_e$ is its yaw rate.

vehicle can be used to predict the baseline without accurate updates from GNSS. As already known from dead reckoning systems, this technique will only give a sufficient accuracy for a certain time, as the integration of sensor errors makes the error in the estimate grow extremely over longer periods time.

For this filter, we extend the state vector to include, along with the two-dimensional baseline and baseline speed, the speed and the heading of the ego vehicle, v_e and ψ_e, and the speed and the heading of the target vehicle v_t and ψ_t:

$$x^k = \begin{bmatrix} b_E & b_N & \dot{b}_E & \dot{b}_N & \psi_e & v_e & \psi_t & v_t \end{bmatrix}^T.$$

The prediction of the baseline is identical to Eq. 12. The prediction of the baseline speed, on the other hand, is modified in a way to incorporate the projection of the speed of each vehicle to the East-North plane by means of its heading. Fig. 8 helps understand the transformation from the local frames of each vehicle to the global East-North frame. The resulting prediction equations are shown next.

$$\begin{aligned}
b_E^{k+1} &= b_E^k + \Delta T \cdot \dot{b}_E^{k+1} + \nu_b \\
b_N^{k+1} &= b_N^k + \Delta T \cdot \dot{b}_N^{k+1} + \nu_b \\
\dot{b}_E^{k+1} &= v_t^k \cdot sin(\psi_t^k) - v_e^k \cdot sin(\psi_e^k) + \nu_{\dot{b}} \\
\dot{b}_N^{k+1} &= v_t^k \cdot cos(\psi_t^k) - v_e^k \cdot cos(\psi_e^k) + \nu_{\dot{b}} \\
\psi_e^{k+1} &= \psi_e^k + \Delta T \cdot \dot{\psi}_e^{k+1} + \nu_\psi \\
v_e^{k+1} &= v_e^k + \nu_v \\
\psi_t^{k+1} &= \psi_t^k + \Delta T \cdot \dot{\psi}_t^{k+1} + \nu_\psi \\
v_t^{k+1} &= v_t^k + \nu_v
\end{aligned} \tag{15}$$

We use the current rotation around the z-axis $\dot{\psi}_e^{k+1}$ to predict the heading of the vehicle ψ_e^{k+1}. The rotation around the z-axis is taken from an inertial measurement unit (IMU) that is mounted inside each vehicle. The IMU measures the acceleration and the turn rate of the vehicle in each axis. When the vehicle is at a standstill a no-rotation assumption is made and the turn rate bias in each of the axis is estimated. This estimation is used to correct the outcome of the turn rate sensor before performing the integration in each time step. The IMU is assumed to be perfectly aligned with the vehicle's axis through an initial calibration procedure.

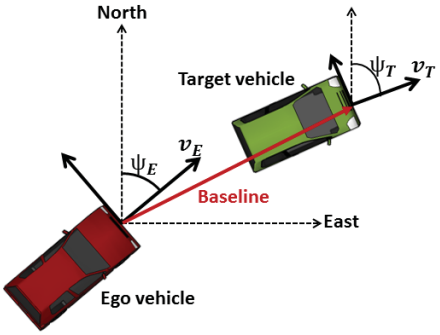

Fig. 8. The baseline is estimated in the local East-North coordinate frame, while speed is given in a vehicle-fixed coordinate frame. By means of the heading, the speed of the vehicle can be transformed from the vehicle-fixed to the local coordinate frame and might be used to stabilize the baseline estimate.

The baseline and the baseline speed are updated as in Eq. 13 and Eq. 14. The speed of each car is updated directly with the speed measurements coming from the vehicle's Controller Area Network (CAN) bus. The vehicle's heading is updated with the heading given by the GNSS receiver.

$$\begin{aligned}
CAN_e^k &= v_e^k + \eta_{CAN} \\
CAN_t^k &= v_t^k + \eta_{CAN} \\
HEA_e^k &= \psi_e^k + \eta_{HEA} \\
HEA_t^k &= \psi_t^k + \eta_{HEA}
\end{aligned} \tag{16}$$

We see that in this filter the prediction equations are not linear in the estimated states. This entails that we cannot build it as a KF, but instead, have to choose one of the suboptimal options that exist. For this work we have chosen to implement this filter as a UKF. Further information regarding its implementation can be found in [15]. Additionally, one constraint to the filter has been implemented. We have chosen to disconnect the GNSS measurements in the update step when the vehicles are at a standstill. Specially in urban environments this has proven to be useful to avoid that corrupted pseudorange and Doppler measurements degrade the baseline estimate. As soon as the vehicle's speed is above a certain threshold the state is again updated with the double differences. In the following section we will test the performance of the multisensor fusion against the PRD-KF approach.

V. Real-World Experiments

In order to assess the pseudorange differentiation and its applicability to real-world traffic scenarios, a series of experiments have been performed. First, we will describe the experimental setup in our two test vehicles, as well as the used reference system for relative positioning and the scenarios where the measurements were acquired. We will then present the results for the test runs for APD, PRD and both Bayesian filters, the PRD Kalman filter (PRD-KF) and the multisensor fusion (MSF) approaches.

A. Experimental Setup

The measurements were performed using two test vehicles. Each vehicle is equipped with a ublox LEA-4T GPS receiver. The GPS receiver is configured to output GNSS raw data such

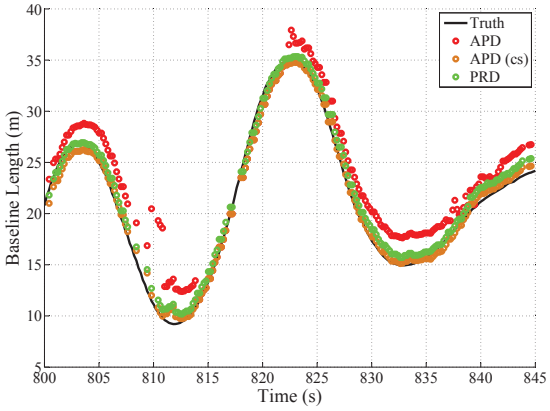

Fig. 9. This figure compares APD with all satellites, APD using only common satellites and PRD with each other.

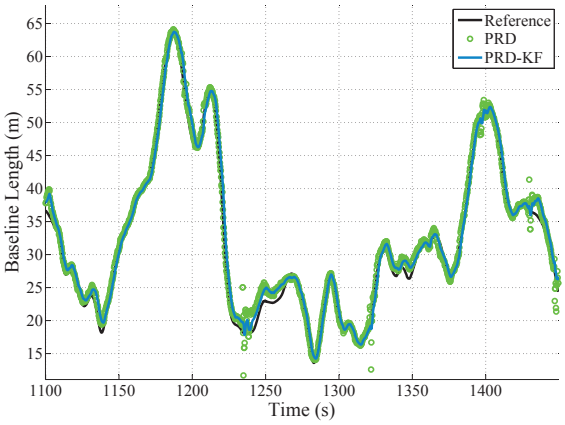

Fig. 10. The figure shows the baseline distance between two vehicles driving on a highway estimated epoch-by-epoch with PRD and filtered with PRD-KF. Short multipath effects in PRD are filtered correctly by PRD-KF.

TABLE I. HIGHWAY SCENARIO

Relative Positioning	Mean Distance Error (m)	Max Distance Error (m)
APD	2.45	20.68
APD (cs)	1.18	17.46
PRD	1.17	17.08
PRD-KF	0.73	3.5
MSF	0.78	3.2

as pseudoranges, Doppler and carrier phase measurements at 4 Hz. A patch antenna is located on the roof of each vehicle. Additionally, an MTx IMU from Xsens is installed in each vehicle. The IMU outputs the measurements from the 3-axis accelerometer and 3-axis gyroscope at a rate of 100 Hz. The IMU is attached rigidly to the chassis of the car. The CAN bus of each vehicle is read out for the speed from the on-board speedometer. The speed information is available at a rate of 10 Hz. All measurements from the sensors are logged on-board on an automotive computer. The data is processed and evaluated offline using MATLAB.

As explained in the introduction, the use-case that motivates this work is the concept of cooperative positioning, which implies that, to some extend, information is exchanged between the participants. The use of a car-2-car communication link would entail further challenges, as for example, the loss of packets or the limited transmission rate. However, this interesting issues fall out of the scope of the present work and we assume that all information from the target vehicle is immediately available at the ego vehicles.

B. Reference System

As a reference system for the relative position between the two vehicles we have chosen an LD-MRS automotive laser scanner from Sick. The laser scanner detects objects in its range of view and tracks their position and their speed. The scanner outputs a list of detected objects every 80 ms. The use of the laser scanner as a reference system has some important advantages, but also some drawbacks [16]. Many research groups favor the use of an INS/GNSS approach to find the ground truth of each vehicle [6], [5], [17]. In many cases, these systems are augmented by the use of Real-Time-Kinematic (RTK) and dual frequency reception. The GNSS carrier phase based positioning solution can reach subcentimeter accuracies in open sky conditions. However, these systems are extremely sensitive and are easily disturbed by satellite signal obstructions, falling back to a pseudorange-only solution. The INS is able to track the position for some time but the errors might grow quickly to the order of meters if no fix on the carrier phase is achieved. The laser scanner is not dependent on good GNSS signal reception and, thus, presents an orthogonal measuring device to the system under test. There are, however, some limitations that we would like to mention. The laser scanner is only able to give a ground truth if the target vehicle drives in front of the ego vehicle in the range of view of the sensor. This is the case up to a separation of 80 meters. Additionally, the laser scanner provides a position of the target vehicle relative to the ego vehicle's reference frame. Our baseline, however, is estimated in the East-North coordinate frame. As shown in Fig. 8 both frames are related through the heading of the ego vehicle. Since a reference for this angle is not known to us, we will only consider the length of the baseline, i.e. the distance between the vehicles and disregard the angle between the baseline and the forward direction of the ego vehicle. The laser scanner has a negative offset when compared to the baseline between the GNSS antennas, since it measures the distance between the front part of the ego-car where the scanner is mounted and the rear part of the target-car. We calibrated this offset before the measurement run, by measuring the exact distance between the GNSS antennas using a handheld laser distance meter. In our case, this offset was 1.07 m.

C. Scenarios

Our test vehicles drove in two different scenarios. First, 30 minutes on a two lane highway were tested. The environment comprises fields, forests or noise protection walls next to the highway. Bridges and overhead direction signs are overhead obstacles that can be encountered. Then, an urban scenario is regarded. In this environment the vehicles drove in the city of Munich, Germany, on larger avenues, as well as narrow streets surrounded by 4 to 6 story high buildings.

TABLE II. URBAN SCENARIO

Relative Positioning	Mean Distance Error (m)	Max Distance Error (m)
APD	4.82	53.48
APD (cs)	2.37	30.77
PRD	2.16	29.12
PRD-KF	1.27	8.65
MSF	1.31	6.83

D. Results

Highway

Both vehicles were driving for approximately 30 minutes on a highway. Fig. 9 shows a 50 second period. In black the reference from the laser scanner is depicted. The red and the orange curves are the APD solutions, once with all available satellites at each receiver and once only using the common satellites. APD uses a least squares and no atmospheric errors are modeled nor corrected. The green curve represents the solution using PRD. We see that between 815 and 820 seconds both APD methods yield the same solution. Here, both receivers use the same satellites and the solution is equivalent to use PRD. However, if one of the receivers uses one different satellite to compute its absolute position the baseline estimate with APD might be off for some meters, as for instance between 830 and 840 seconds. This matches our results from Section III. Table I summarizes the mean errors for the 30 minute drive. We see that, in fact, the difference between the mean values of APD and APD with only common satellites is below two meters. This can be explained due to the fact that on the highway good satellite coverage exists and most of the time both receivers track the same satellites. Multipath propagation due to overhead bridges and noise protection walls are responsible for the larger errors in the PRD solution.

Fig. 10 shows the improvement of using the Kalman filter on the pseudoranges the baseline length between both vehicles for a 6 minute section on the highway. The green dotted curve is the solution with PRD with all satellites common to both receivers and above 10 ° elevation. In Table I the Bayesian approaches are compared to the PRD snapshot approach. We see how the PRD-KF filter smooths the errors in PRD caused by multipath propagation and low signal strength when driving under bridges, as for example in second 1240.

The mean values in Table I give the impression that the multisensor fusion technique MSF does not offer a major improvement over the PRD-KF filter. Its strength is in attenuating outliers in the baseline estimate due to multipath effects on the pseudoranges and to offer continuity in GNSS denied scenarios. Specially the later we demonstrate in Fig. 11 by switching off the measurements from the GNSS receivers for a period of 4 minutes on a highway. We see how from second 1300 on the PRD-KF prediction quickly diverges according to the constant velocity movement model, whereas the MSF filter is able to track the baseline until second 1550 when the GPS measurements are again available.

Urban

The urban environment presents the most challenging of the chosen scenarios, due to the impact of multipath on the pseudorange and Doppler measurements in each of the receivers. The measurements might be off by tens of meters, causing a corresponding error on the baseline estimate. In

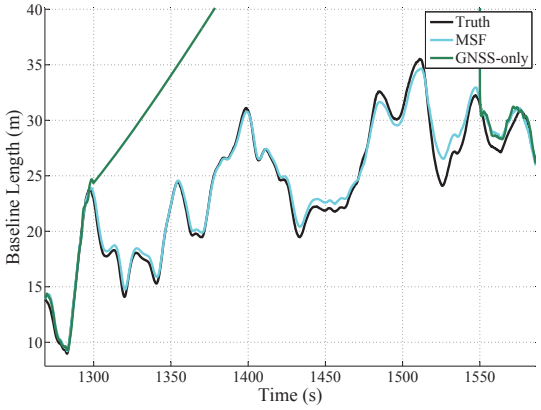

Fig. 11. Section of the highway scenario. From second 1300 to 1550 the GPS measurements are disconnected and the baseline in MSF is estimated only using on-board sensors.

Fig. 12 we show a 220 seconds snapshot in the city of Munich. Specially around second 300 major errors in PRD can be appreciated. In this moment the vehicles are driving in an urban canyon with large buildings at both sides. The PRD-KF filter partly reduces the impact of the high peaks produced by the multipath affected pseudoranges. Errors above five meters can still be appreciated. Fig. 13 shows the comparison between the PRD-KF filter and the MSF approach. With the help of the on-board sensors we are able to lower the impact of multipath errors on the baseline estimate and have a better tracking of the target vehicle's position.

The mean values for the urban scenario are given in Table II. We can see the characteristic large outliers for this environment. As in urban environments it is more likely that each receiver is tracking a different set of satellites, the mean value of PRD, on average, is smaller than APD. PRD-KF is able to further decrease the error of PRD by smoothing the outliers. The resulting mean baseline error is below 1.5 m. Again, we see how MSF decreases the error peaks, but in the long run its mean does not show an improvement over the PRD-KF approach.

In the urban experiment the measurement covariance matrices R_ρ and R_Φ were set with large values in order not to count strongly on the corrupted GNSS measurements and rely more on the on-board sensors. The on-board sensors, however, do not provide information of the relative position of the target vehicle, but help in predicting the position of each of the vehicles. This fact will lead to an inevitable increase of the error in the baseline estimate if no uncorrupted pseudorange double difference measurements are supplied. Therefore, it is of highest importance to distinguish when uncorrupted double differences are available and readjusting the covariance matrices R_ρ and R_Φ accordingly, in order to increase again the belief in the baseline estimate. The detection of GNSS blockage and corrupted double differences is left as future work.

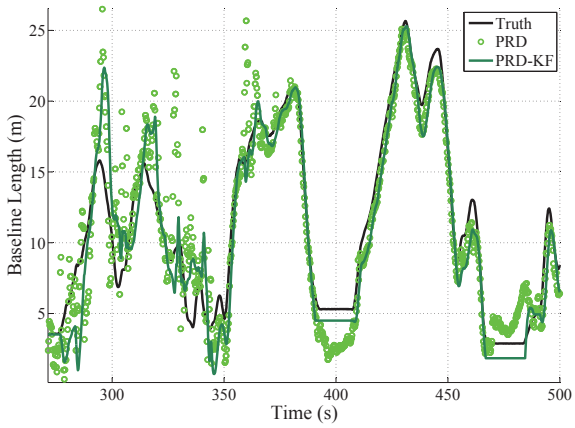

Fig. 12. The figure shows the baseline distance between two vehicles driving in an urban environment.

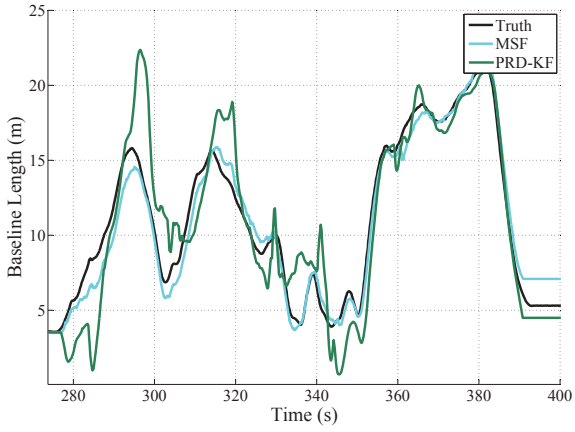

Fig. 13. The figure shows the baseline estimated with GNSS only (PRD-KF) and with the multisensor fusion (MSF) approach.

VI. Conclusion

In this paper we analyzed the use of GNSS double differenced pseudoranges to estimate the relative position of two vehicles. From a theoretical point of view, we compared the pseudorange differencing approach to the subtraction of absolute positions. We learned that the performance of both methods depends on the magnitude of the common errors on the pseudoranges of both receivers and on the magnitude of the pseudorange noise. The number of satellites used in each receiver, as well as the constellation geometry, have a direct impact on which of the two approaches yields a smaller baseline error.

We described two Bayesian filters that make use of pseudorange double differences to track the position of a target vehicle. First, a Kalman filter approach using pseudorange and Doppler measurements revealed acceptable results in estimating the distance to a foregoing car while driving on a highway and in an urban environment. It effectively smoothed out errors caused by reduced signal strength and multipath propagation. This filter was extended to incorporate the information from on-board sensors, such as an inertial measurement unit and a speedometer. This multisensor fusion approach yielded promising results in GNSS-degraded environments by maintaining a bounded relative position estimate.

The detection of impaired pseudorange measurements to mitigate their impact on the relative position estimate and the dynamic adjustment of the GNSS measurement noise covariance matrices are left as future work.

References

[1] ETSI TS 102 637-2, "Intelligent Transport Systems (ITS) - Vehicular Communications - Basic Set of Applications - Part 2 : Specification of Cooperative Awareness Basic Service," tech. rep., ETSI, 2010.

[2] E. Richter, M. Obst, R. Schubert, and G. Wanielik, "Cooperative relative localization using vehicle-to-vehicle communications," in *Information Fusion, 2009. FUSION '09. 12th International Conference on*, pp. 126 –131, july 2009.

[3] D. Yang, F. Zhao, K. Liu, H. B. Lim, E. Frazzoli, and D. Rus, "A GPS Pseudorange Based Cooperative Vehicular Distance Measurement Technique," in *VTC Spring*, pp. 1–5, IEEE, 2012.

[4] N. Alam, A. Balaei, and A. Dempster, "Positioning Enhancement with Double Differencing and DSRC," in *Proceedings of the 23rd International Technical Meeting of The Satellite Division of the Institute of Navigation (ION GNSS 2010)*, (Portland, OR), pp. 1210–1218, September 2010.

[5] N. Alam, A. Tabatabaei Balaei, and A. G. Dempster, "Relative Positioning Enhancement in VANETs: A Tight Integration Approach," *Intelligent Transportation Systems, IEEE Transactions on*, vol. PP, no. 99, pp. 1 –9, 2012.

[6] M. Obst, E. Richter, and G. Wanielik, "Accurate Relative Localization for Land Vehicles with SBAS Corrected GPS/INS Integration and V2V Communication," in *Proceedings of the 24th International Technical Meeting of The Satellite Division of the Institute of Navigation (ION GNSS 2011)*, pp. 363–371, 2011.

[7] F. de Ponte Müller, A. Steingass, and T. Strang, "Zero-Baseline Measurements for Relative Positioning in Vehicular Environments," in *Proceedings of the 6th European Workshop on GNSS Signals and Signal Processing*, 2013.

[8] S. Zeng, "Performance Evaluation of Automotive Radars Using Carrier-Phase Differential GPS," *IEEE Transactions on Instrumentation and Measurement*, vol. 59, pp. 2732–2741, Oct. 2010.

[9] N. Luo, "Precise Relative Positioning of Multiple Moving Platforms Using GPS Carrier Phase Observables," 2001.

[10] S. Martin, W. Travis, and D. Bevly, "Performance Comparison of Single and Dual Frequency Closely coupled GPS/INS Relative Positioning Systems," in *Position Location and Navigation Symposium (PLANS), 2010 IEEE/ION*, pp. 544–551, May 2010.

[11] P. Misra and P. Enge, *Global Positioning System: Signals, Measurements, and Performance*. Ganga-Jamuna Press, Lincoln MA, 2nd edition ed., 2006.

[12] G. Strang and K. Borre, *Linear Algebra, Geodesy, and GPS*. Wellesley-Cambridge Press, 1997.

[13] J. Breu, A. Brakemeier, and M. Menth, "Analysis of Cooperative Awareness Message rates in VANETs," in *ITS Telecommunications (ITST), 2013 13th International Conference on*, pp. 8–13, Nov 2013.

[14] B. Kloiber, T. Strang, M. Rockl, and F. de Ponte-Muller, "Performance of CAM based safety applications using ITS-G5A MAC in high dense scenarios," in *Intelligent Vehicles Symposium (IV), 2011 IEEE*, pp. 654–660, June 2011.

[15] S. J. Julier and J. K. Uhlmann, "A New Extension of the Kalman Filter to Nonlinear Systems," pp. 182–193, 1997.

[16] F. de Ponte Müller, L. M. Navajas, and T. Strang, "Characterization of a Laser Scanner Sensor for the use as a Reference System in Vehicular Relative Positioning," in *Communication Technologies for Vehicles*, pp. 146–158, Springer Berlin Heidelberg, 2013.

[17] M. Petovello, K. O'Keefe, and B. Chan, "Demonstration of inter-vehicle UWB ranging to augment DGPS for improved relative positioning," in *Proceedings of IEEE/ION GNSS 2010*, 2010.